Characterization of the focal plane of the microchannel X-ray telescope at the metrology beamline of SOLEIL synchrotron for the space astronomy mission SVOM

Aline Meuris, Benjamin Schneider, Hugo Allaire, David Baudin, Ion Cojocari, Paulo da Silva, Eric Doumayrou, Diego Götz, Philippe Ferrando, Philippe Laurent, et al.

Characterization of the focal plane of the Microchannel X-ray Telescope at the Metrology beamline of SOLEIL synchrotron for the space astronomy mission SVOM

1. Introduction

1.1 Scientific context

The SVOM mission to be launched in 2023 by the Chinese Academy of Science is an observatory dedicated to the time-domain astrophysics and in particular the study of the gamma-ray bursts. Gamma-ray bursts are brief flashes of gamma rays, appearing in random directions in the sky. They are produced by the death of massive stars or the coalescence of compact binary systems. They are characterized by a prompt emission in the gamma-ray range followed by an afterglow emission in all wavelengths of the electromagnetic spectrum. The SVOM mission is composed of a satellite with 4 instruments and 3 ground-based telescopes for the follow-up (see Figure 1). Onboard the satellite, the Microchannel X-ray Telescope (MXT) will rapidly refine the location error box of the transient source detected by the wide field of view instrument ECLAIRs and will observe the afterglow in the 0.2 to 10 keV energy range. MXT is developed by a European collaboration under the responsibility of the French Space Agency (CNES) [1]; it is a focusing X-ray telescope of 1.15 m focal length with time-resolved spectroscopy capability [2]. It is composed of a microchannel-pore-based optics, a telescope structure, a radiator, a camera [3] and a data processing unit, for a total mass of 35 kg and a power of 60 W.

1.2 Motivations for a characterization campaign

In the camera, the detection chain is based on a 256 x 256 pixels pnCCD for X-ray imaging spectroscopy, read out by CAMEX analog ASIC, both provided by the Max-Planck-Institute for Extraterrestrial Physics (see Figure 2). This system is similar to the camera development for the eROSITA instrument on-board the Spektrum Roentgen Gamma mission [4]. There are nevertheless two major design differences. On one hand, the optical on-chip filter has not the same composition and so the quantum efficiency (QE) cannot be inferred from eROSITA QE calibration. On the other hand, the warm front-end electronics is a new US-free design which performance in terms of noise and linearity shall be characterized.

Three space-grade focal planes were produced and characterized in a full-custom cryostat. An X-ray source was developed with an X-ray tube and a composite fluorescence target to produce X-ray lines from 1.5 keV to 9 keV (see Figure 3). This allows a rapid energy calibration over the whole energy range and the evaluation of the energy resolution, especially at 1.5 keV which the scientific requirement of the instrument is specified. However, the crucial energy response of the camera where the MXT optics is the most sensitive (< 2 keV) was only characterized by one line (Al-K) produced by the X-ray tube. In addition, the simultaneous presence of several spectral lines associated to

the Bremsstrahlung continuum spectrum induced by the X-ray tube introduce uncertainties in the energy calibration and energy resolution determination. Finally, the evaluation of the charge transfer efficiency (CTE) might be overestimated in the case of a bright and uniform illumination of the detector (e.g., the X-ray tube) compared to very low flux astrophysics sources that MXT will detect in flight. For a bright and uniform source, electron traps are more likely to be filled by existing charges, which reduced the probability of trapping during the charge transfer. To address these questions, we carried out a test campaign at the Metrology beamline of SOLEIL synchrotron and further characterized the spectral response of the MXT camera at E < 2 keV. This facility offers three fundamental characteristics for this objective. First, the monochromatic beam, tunable from 40 to 1800 eV, allows for energy calibration and characterization of the spectral resolution. Then, the focused beam allows local illumination of selected areas of the detector to determine the CTE. Finally, the knowledge of the absolute flux sent onto the detector allows for quantum efficiency evaluation.

2. Experimental setup

2.1 Metrology beamline and MXT setup

The Soft X-ray branch of the Metrology Beamline uses the radiation emitted by a bending magnet (see Figure 4). It covers an energy range between 40 and 1800 eV with few 10^9 photons/s in a 250 $\times$ 120 µm² FWHM focused beam. The typical spectral resolution is about a few tenths of eV. A low order sorter is used for rejection of the monochromator higher order harmonics to reach a spectral purity better than 99 % over the whole energy range.

We adapted the existing Focal Plane Assembly (FPA) cryostat for interfacing with the Metrology beamline. Initially, for the first characterization in the laboratory, the cryostat was equipped with a liquid nitrogen (N_2L) tank above the functional part holding the FPA; a thermal link with a heater was connected to the FPA shielding to control the detector temperature from -100°C to room temperature. The cryostat was 178 cm high with an optical axis at 74 cm. In the soft X-ray experimental hutch of the beamline, the beam output height is 173 cm with respect to the floor, for a ceiling height of 200 cm. Consequently, the cryostat was vertically rotated to get the functional part on top and the N_2L tank was replaced by a baseplate filled with coolant fluid controlled by a cryocooler. We designed a mechanical structure for the cryostat to be used as a trolley and to hold the cryostat with 6 degrees of freedom for the alignment on the X-ray beam. Inside the cryostat, the FPA was fixed to two displacement tables to allow the scan of the detector in front of the beam.

The system characterized at SOLEIL is the flight spare model of the MXT detection channel, i.e., the flight spare model of the focal plane assembly inside the cryostat and the flight spare model of the front-end electronics assembly outside the cryostat. All parts of the flight spare models come from the same production batches as the flight models.

So the global trends and results are applicable to the flight model but some special features (noisy pixels…) can be device dependent.

2.2. MXT implementation and beamline settings

The nominal photon flux of the beamline is far too high to operate the detector without event pile-up in the pixels of 75 µm × 75 µm: 10^8 photons/s/pixel for a detection system reading out 10 frames per second. The target count rate for adequate photon counting and spectroscopy should not exceed 1 count/pixel/second (see pile-up assessment in [5]), meaning a required flux reduction of 8 orders of magnitude. This challenge in the photon flux reduction was addressed by several means: (i) the distance between the X-ray beam focal spot and the detector to take benefit of the beam output divergence, (ii) the reduction of the monochromator exit slits opening and (iii) the use of additional X-ray filters combined with a higher rejection of the monochromator higher-order harmonics.

The beam divergence is 1 mrad in the horizontal plane (i.e., in the charge transfer direction of the CCD) and 0.3 mrad in the vertical one (i.e., along the columns of the CCD). The full length of the casemate was used to place the detector 5 meters downstream of the beamline exit. As a result, while impinging the detector, the beam spot has an expected size of 5.2 mm × 1.6 mm (~300 times the initial surface), corresponding to illuminate 70 columns and 20 rows of the image area. This method provides a surface flux reduction by a factor of 300. The monochromator exit slits, which are nominally opened at 100 µm, could be adjusted as well to only few µm leading to a further flux reduction per pixel. Calibration tests of the slits apertures have been made in the past to demonstrate the proportionality between the slit opening reduction factor and the flux reduction factor. Both methods allowed to reduce by 4 to 5 orders of magnitude the photon flux per pixel. To gain the 3 to 4 other orders of magnitude needed for pile-up reduction, additional X-ray filters can be placed in the last beamline chamber. Filters with different materials and thicknesses were placed on a motorized frame to cover the energy range from 200 to 1800 eV. However, the use of strong absorbing filters leads to beam hardening and a higher level of contamination from undesired higher energies. Thus, rejection power of the beamline Low-Order Sorter was increased accordingly to maintain the output beam spectral purity.

As given in Table 1, settings of the beamline were adjusted from 300 eV to 1800 eV to provide monochromatic beam with the desired flux and spectral purity on the detector. The requirement was to detect less than 1 % of the incident flux at twice the working energy, ensuring both good harmonics rejection and no pile-up in the detector. This working condition was obtained in any of the settings below. The resulting images and spectra at few energies are illustrated in Figure 6. Beam settings that satisfied our spectral and counting requirements were not found during the campaign between 200 eV and 300 eV. This is due to the difficulty to reject the higher-order harmonics when they start at rather low energy (400 to 600 eV).

3. Data analysis methods

3.1 Spectral analysis

When an X-ray photon interacts in the pnCCD, it creates, by photoelectric effect, charges that drift underneath the pixel electrodes and are stored until the readout of the frame. Due to charge diffusion in the semiconductor detector during the charge drift, the total charge can be shared on up to 4 neighboring pixels. In each frame, the front-end electronics detects the pixels whose amplitude is above a configurable low-level threshold and sends their pixel coordinates and amplitude information (corresponding to the collected charge) to the downstream processing. The MXT analysis pipeline consists in converting this list of hit pixels to a list of photon events. This requires a processing step of event clustering: the pixel clusters shall be identified and the amplitudes in each pixel of the cluster shall be summed after individual energy calibration. As a result, our detection and acquisition system record the photon time of arrival, the photon position, the photon energy. The time resolution is the frame integration time of 100 ms. The spatial resolution is the pixel size of 75 µm (coordinates of the pixel recording the biggest charge); a finer position estimate would be possible with a barycentric method but is not implemented in the analysis software due to the final use of the detector (focal plane of a 10 arcmin angular resolution telescope, the point spread function is ~ 45 pixels diameter wide at FWHM). The energy resolution is energy dependent and multiplicity dependent and is discussed here after. From this list of events, we can compute cumulative photon count maps (images) and histograms of amplitudes or energy with an a priori calibration table (spectra), as illustrated in Figure 6. This calibration table were obtained during the pre-campaign measurements in our laboratory using the X-ray source with multiple spectral lines. During the test campaign, a quicklook version of this pipeline was used to extract single events and display their spectra. The algorithm simplifies the pattern recognition step by avoiding the time-consuming event clustering process. Multiple hit events are so rejected from this quick analysis. This speeds up the process by a factor of 10 while maintaining a sufficient quality of the reduced products (count map, spectra). During the tuning phase of the beam, this online analysis was crucial to determine the spectral purity and validate the beamline configuration. After the test campaign, a complete offline analysis was performed. The energy calibration was refined using a dataset of one spot position on the detector. The new calibration table was in good agreement with the initial reference table used for the quicklook analysis. As a consequence, for the analysis concerning the energy resolution and the charge transfer efficiency, we decided to use the initial calibration tables obtained with the X-ray tube source based on more event statistics over the full matrix.

3.2 Photon counting analysis

The photometric analysis consists in several computing steps. First, the beam flux (number of X-ray photons, N_0, per second) is obtained from the beam current measured by a reference diode (equation 1). The 10 mm × 10 mm diode fully intercepts the 240 µm × 120 µm beam at the focal spot; the 19.2 mm × 19.2 mm detector fully intercepts the 5.2 mm × 1.6 mm beam after divergence in vacuum. N_0 is calculated from the diode current I_D with the following formula (valid only for a monoenergetic beam of energy E):

$$I_D(A) = q \times N_0 \times T_{Al}(E) \times \frac{E}{\varepsilon} \qquad (1)$$

where q is the charge of the electron, T_{Al} is the transmission of the 150 nm aluminum coating of the diode and ε is the averaged pair creation energy in silicon at room temperature. This transmission can be obtained by calibration and is known with a 5 % precision; ε was measured in the literature between 3.62 and 3.65 eV (1 % precision) [6].

Secondly, we derive the photon flux (N_I) impinging on the MXT detector by taking into account the differences in the beamline settings used for the diode and the MXT measurements for each energy run:

$$N_I = N_0 \times \frac{I_M}{I_{M0}} \times \frac{H_{PB}}{H_{PB0}} \times T_{FE} \times F \qquad (2)$$

where I_M and I_{M0} are the synchrotron machine current intensities during MXT and diode measurements respectively, H_{PB} and H_{PB0} are the transfer functions of the low-pass filter for the angle used in the MXT measurement and in the diode measurement respectively, T_{FE} the transmission of the external filter only used during the MXT measurement, and F the ratio of the openings of the slits between the MXT and the diode measurements. The machine current is stable within 0.5 % so its correction is not necessary at first order. The transfer functions are computed by simulations of the optical system; when we operate the diode and the MXT detector with the same low-pass filter angle, the uncertainties only depend on how reproducible the angle and the energy can be set, and are estimated below 5%. After calibration of the external filters, the remaining uncertainty on the transmission T_{FE} comes from the modeling of the transmission and the knowledge on the absolute energy and is evaluated to be lower than 10%. The absolute opening of the slits is known with 0.2 µm precision; so, for some configurations with small openings, the error can reach 10%. Thirdly, we extract the number of events per second N_D recorded in the detector after pixel clustering. Measurement duration is defined to collect at least 20000 photons to limit the measurement error due to the Poisson statistics to 1 %. Looking at the spectral distribution of the events, we estimated the photon pile-up to 1 % and the pattern pile-up to 5%. Finally, we compute the ratio between the detected and the incoming fluxes to obtain the quantum efficiency (QE):

$$QE = \frac{N_D}{N_I} \qquad (3)$$

Taking into account all (independent) uncertainties, we expect an error on QE between 5 and 20 %.

4. Experimental results

4.1 Event statistics

The event multiplicity, i.e., the number of hit pixels per photon event, was characterized at low energy and close to the threshold of the detection chain (0.2 keV). If we consider a punctual electron charge cloud (true in X-rays) and the diffusion phenomenon only in a planar detector (good approximation in the integration phase of the pnCCD), the spatial distribution of the charge cloud at distance z from the interaction point can be modeled by a 2D-Gaussian of variance:

$$\sigma^2 = \frac{2kTL}{qV} z \qquad (4)$$

where k is the Boltzmann constant, T the operating temperature, L the thickness of the fully depleted detector, V the depletion voltage. The event multiplicity statistics depends on the ratio between the charge cloud size defined by Eq. 4 and the pixel size on one hand, and the ratio between the signal (amplitude of the Gaussian) and the low-level threshold on the other hand. For a given detector geometry and mean low-level threshold, the statistics is thus energy dependent. Such a modeling was applied with eROSITA detector which has the same pixel size (75 µm) and about the same low-level threshold (50 eV versus 46 eV for MXT) [7]. The operating temperature was -60°C in the SOLEIL experiment versus -85°C during the eROSITA calibration campaign, which increases the size of the charge cloud by 6% according to Eq. 4. By adapting this size parameter, we could fairly model the statistics of the event multiplicity measured during the SOLEIL campaign except at 300 eV (see Figure 7). The same model was also applied during the MXT calibration test campaign in the PANTER test facility at -65°C with the same low-level threshold [7]. The deviation at 300 eV is an artefact from the experimental setup. The measurements at low energy (below 400 eV) in SOLEIL synchrotron were corrupted by spurious and numerous low energy events that were not correlated to the photon beam but by the opening of the gate valve fixed on our cryostat; we assume that the holding current of this valve (with a Vatlock system) caused electromagnetic perturbations. This point shall be investigated and corrected for the next test campaign.

4.2 Energy resolution

The energy resolution measured during the campaign is summarized in Figure 8. We obtained typically 88 eV FWHM at 1.5 keV versus 84 eV with the MXT cryostat in the lab in the same configuration. The thermal, vibration and electromagnetic environments in the hutch were likely to be less favorable for the electronic noise. In particular, the operating temperature of the detector had to be set to -60°C instead of -65°C for a long-term use of the cryocooler (96

hours continuous operation). The energy resolution can be modeled with an electronic noise of 7 electrons rms independent of the energy and a Fano factor of 0.13 (see [8] for comparison with the flight configuration).

4.3 Charge transfer efficiency

The energy resolution at various energies was determined in one area of the detector. To address the charge transfer efficiency, measurements were made at three positions on the detector while maintaining the beam in exactly the same conditions (one energy, one flux); the data set are represented overplotted in Figure 9a. The line positions are fitted for each row and are represented as a function of the number of transfer *n* to extract the CTE using the following equation (see Figure 9b):

$$\frac{A(0) - A(n)}{A(0)} = 1 - CTE^n \qquad (5)$$

where A(j) is the mean amplitude (spectral line position in ADU or eV) of events recorded at the detector row #j. The measurement was performed at two energies, 600 and 1000 eV. Data obtained are in agreement with the measurements performed in the laboratory with the composite X-ray source and with the MXT Panter calibration campaign done with the flight model [7](see Figure 10). The dependency of the CTE with energy can be explained by the fact that CTE expresses a ratio of charge loss whereas physically this is a number of charges which is lost depending of the time constants of the traps in the material and the delays to readout the matrix. We can notice than for the two other campaigns, the pixel flux was similar (0.1 ct/pixel/s) to the one in the experiment at SOLEIL but the matrix was fully illuminated. This validates both methods (full and partial illumination) for the determination of the CTE, provided that the flux is low enough. The plan for a next campaign is to improve the system with the displacement table in order to allow a continuous scan of the detector along a column. The goal would be to provide again a global CTE value for the matrix at a given energy but with more row data to better constraint the parameter. The experiment can be reproduced at different energies, and in particular close to the low-level threshold where the charge loss is affected by other effects like the quantum efficiency and the thresholding.

4.4 Quantum efficiency

The Figure 11 presents the results of the data analysis: the flux measured by the diode N_0, the incident flux on MXT N_I and the flux measured by MXT N_D are extracted according to the method detailed in section 3.2. However, by making the ratio between the detected and incident flux we failed in getting realistic values of the quantum efficiency in any of the tested energy bands. The measurement protocol, given the experimental and time constraints, consisted in two (time) independent sets of measurements: on one hand, the diode current measurements for a set of energies sharing the same adequate beam configuration (order-sorter, slits, line internal filter, no external filter) and on the other

hand, the MXT measurements for the same energies with the same beam configuration but with a different slit opening and using an additional external filter (see Table 1). The reproducibility of the Metrology beam is expected to be excellent (precision on the energy better than 0.2 eV and on the angle of the low-pass filter better than 0.001°) so that even if it could happen that the beam configuration parameters were changed in between these two measurements, the same photon flux values are recovered when the parameters were returned to their nominal values. To reduce the uncertainties, we calibrated the attenuation of the external X-ray filters and we performed a new calibration of the reference diode. We refined the data analysis to perform the photon counting in the energy band of the beam only to get rid of spurious events below 200 eV. Despite this work, the results of the computation of the quantum efficiency are far from the expected value for a 450 µm thick silicon detector with a theoretical composition of the on-chip filter of 100 nm Al, 30 nm Si_3O_4 and 40 nm SiO_2. As a conclusion, our test protocol based on indirect reference photon counting is not validated for absolute quantum efficiency measurement. Possible explanations would be bad offset values in the current measurement of the diode or in the opening of the slits (errors in N_0 and F in equation 2). Actually, better results on the composition of this filter were obtained with a Rutherford Backscattering Spectroscopy (RBS) method applied in the JANNuS-SCALP platform in May 2021 [9]; it concludes to a thickness of aluminum of 104 nm $\pm$ 8 nm in 9 regions of the detector. The RBS method was not suited to find localized defaults expected in the aluminum layer and we expected achieving this goal with in the SOLEIL facility. For a second test at SOLEIL Metrology beamline, we plan to scan the detector in the prospect of studying relative variations of quantum efficiency instead of measuring absolute quantum efficiency.

5- Conclusions and perspectives

This paper presents the calibration campaign of the flight spare detection chain of the MXT instrument on the soft X-ray branch of the Metrology Beamline at SOLEIL. This first campaign was technically successful, with the challenges of placing a cryostat at 10^{-6} mbar in the experimental hutch 5 meters downstream from the X-ray beam focal spot. For the first time, the system was continuously operated during 96 hours with a cryocooler and a system of thermo-electric coolers to maintain the detector between -65°C and -60°C. Specific configurations of the beamline were successfully implemented to provide a monoenergetic beam from 300 to 1800 eV with a photon flux reduced to 1 photon/s/pixel while keeping excellent spectral purity. Accurate measurements of the energy resolution and the charge transfer efficiency were obtained below 1 keV, in good agreement with other facilities. Characterizations from 100 to 300 eV could be the goal of a next campaign to better characterize the low-energy threshold of the detection chain. This would require, on one hand, another tuning of the beamline (probably with other external filters) and on the other hand, an upgrade of the MXT set-up to get rid of spurious events at low energy probably caused by the VAT

gate valve. The absolute measurement of the quantum efficiency was not achieved. The absolute flux needs to be measured at the level of 150 ph/s in the same beamline configuration and optical setup than for the MXT measurements. Such measurements can only be achieved with cryo-cooled X-ray bolometers. However, to answer the question of the uniformity of the aluminum on-chip filter, we can contemplate for a next campaign the possibility of a relative measurement of the quantum efficiency by scanning the full detector surface at one or two energies. Another interesting perspective of this work would be to measure again the energy resolution and the charge transfer efficiency of this specimen after proton irradiation, in order to predict the performance in flight of the focal plane assembly of MXT on board SVOM.

References

[1]. K. Mercier, F. Gonzalez, D. Götz et al., "Results of the development of the MXT X-ray telescope for the SVOM Mission", SPIE Proc., Vol. 12181 (2022), 12181-64.

[2]. D. Götz et al., "The Scientific Performance of the Microchannel X-ray Telescope on board the SVOM mission", submitted in Experimental Astronomy.

[3]. A. Meuris et al., "Design and performance of the camera of the SVOM Micro-channel X-ray Telescope", submitted in Nucl. Instruments and Methods section A.

[4]. N. Meidinger et al, "Development of the focal plane PNCCD camera system for the X-ray space telescope eROSITA", Nuclear Instruments and Methods in Physics Research Section A: Volume 624, Issue 2, 2010, Pages 321-329, https://doi.org/10.1016/j.nima.2010.03.126.

[5]. J. Ballet, "Pile-up on X-ray CCD instruments." *Astronomy & Astrophysics Supplement Series* 135 (1999): 371-381

[6]. P. Lechner, R. Hartmann, H. Soltau, L. Strüder, "Pair creation energy and Fano factor of silicon in the energy range of soft X-rays," Nuclear Instruments and Methods in Physics Research Section A: Accelerators, Spectrometers, Detectors and Associated Equipment, Volume 377, Issues 2–3, 1996, Pages 206-208, https://doi.org/10.1016/0168-9002(96)00213-6.

[7]. K. Dennerl et al., "Determination of the eROSITA mirror half energy width (HEW) with subpixel resolution," SPIE Proc., Vol. 8443 (2012), 844350.

[8]. B. Schneider, "Spectral performance of the MXT flight camera on board the SVOM mission", submitted to Experimental Astronomy.

[9]. C.-O. Bacri, C. Bachelet, C. Baumier et al., “SCALP, a platform dedicated to material modifications and characterization under ion beam”, Nuclear Instruments and Methods in Physics Research Section B, Volume 406, Part A, 2017, Pages 48-52, https://doi.org/10.1016/j.nimb.2017.03.036.

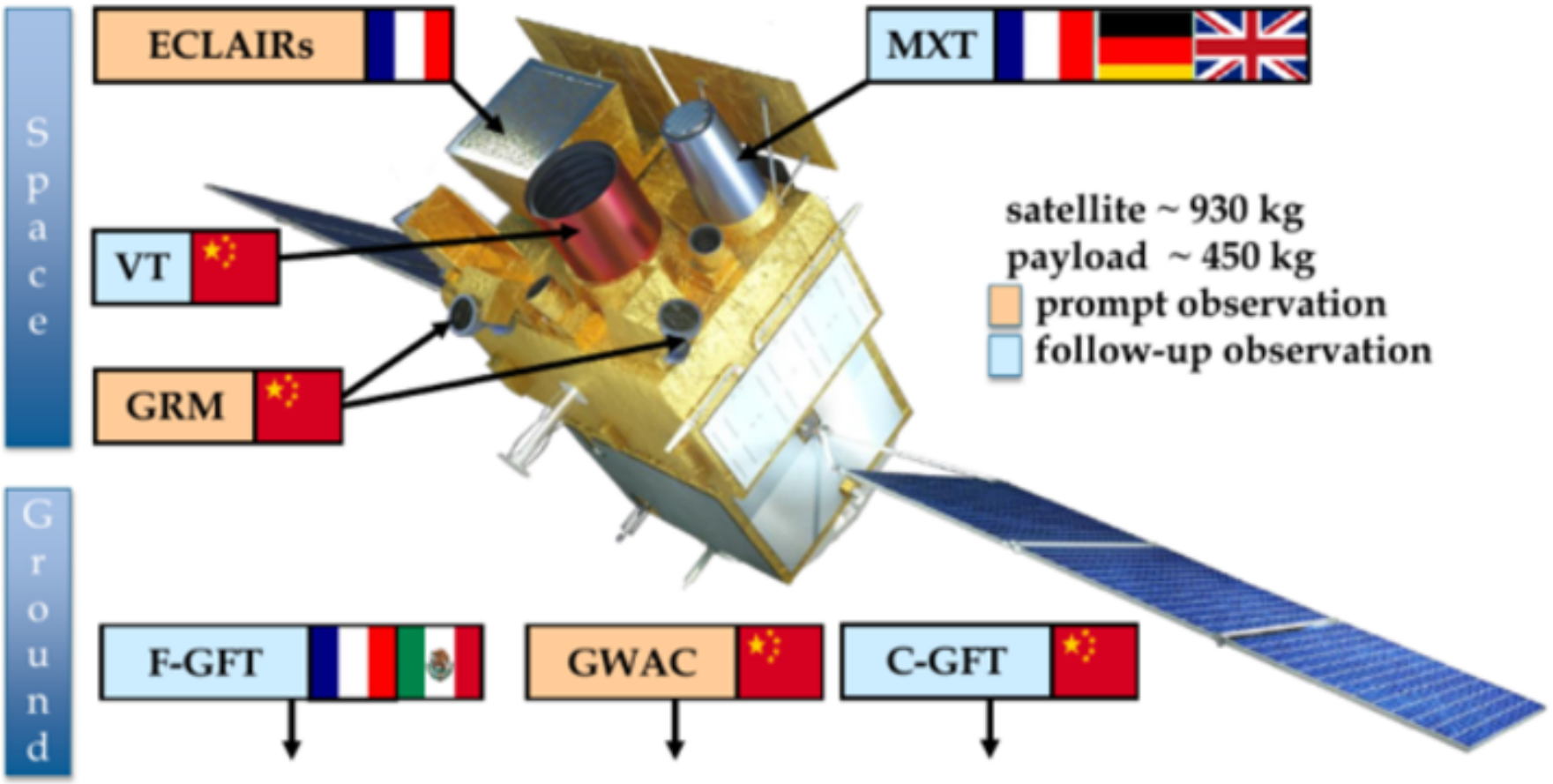
Space
Ground
ECLAIRs
MXT
VT
GRM
satellite ~ 930 kg
payload ~ 450 kg
prompt observation
follow-up observation
F-GFT
GWAC
C-GFT

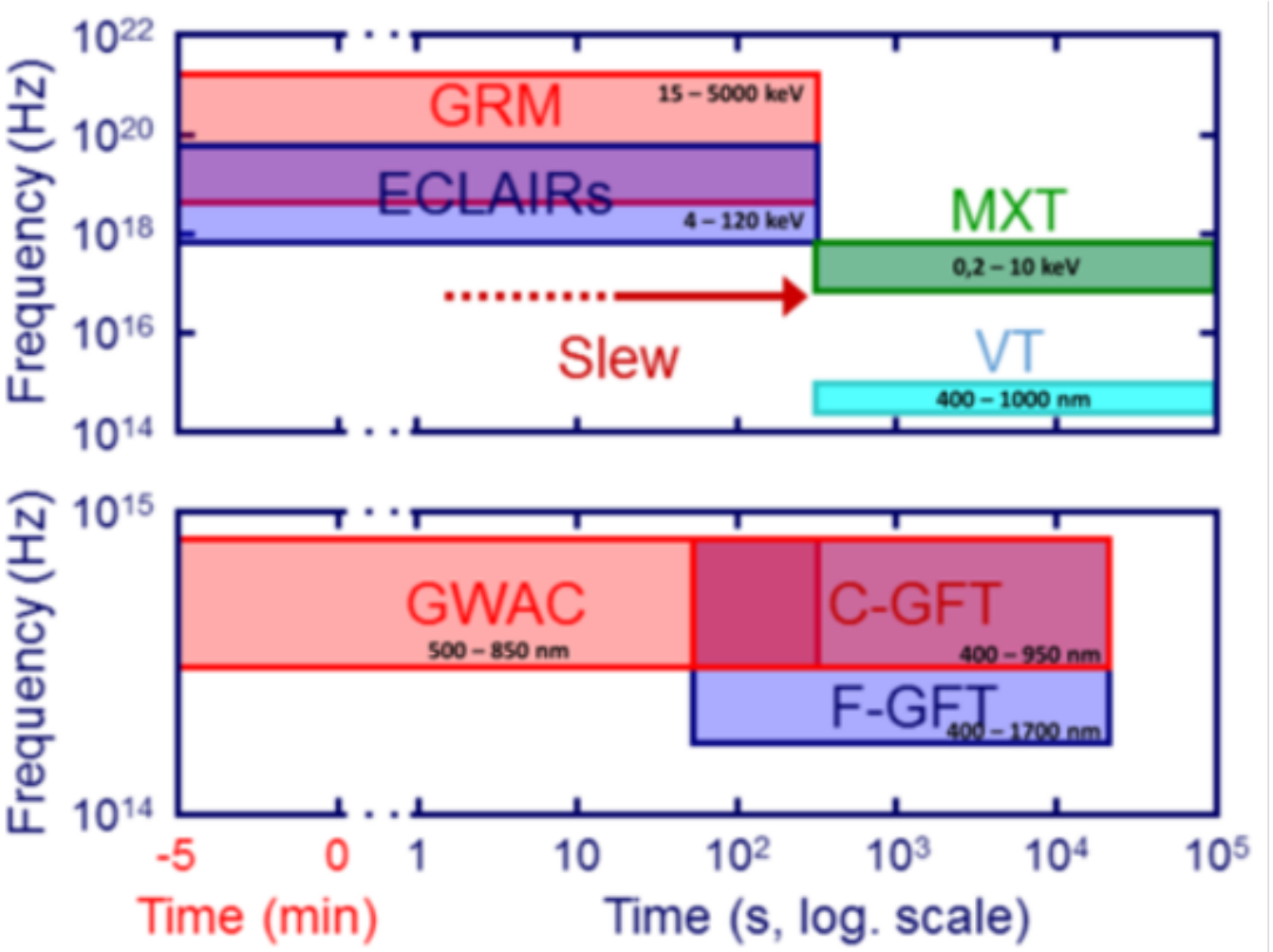
Frequency (Hz)
10^22
10^20
10^18
10^16
10^14
GRM
15 – 5000 keV
ECLAIRs
4 – 120 keV
MXT
0,2 – 10 keV
Slew
VT
400 – 1000 nm
Frequency (Hz)
10^15
10^14
GWAC
500 – 850 nm
C-GFT
400 – 950 nm
F-GFT
400 – 1700 nm
-5
0
1
10
10^2
10^3
10^4
10^5
Time (min)
Time (s, log. scale)

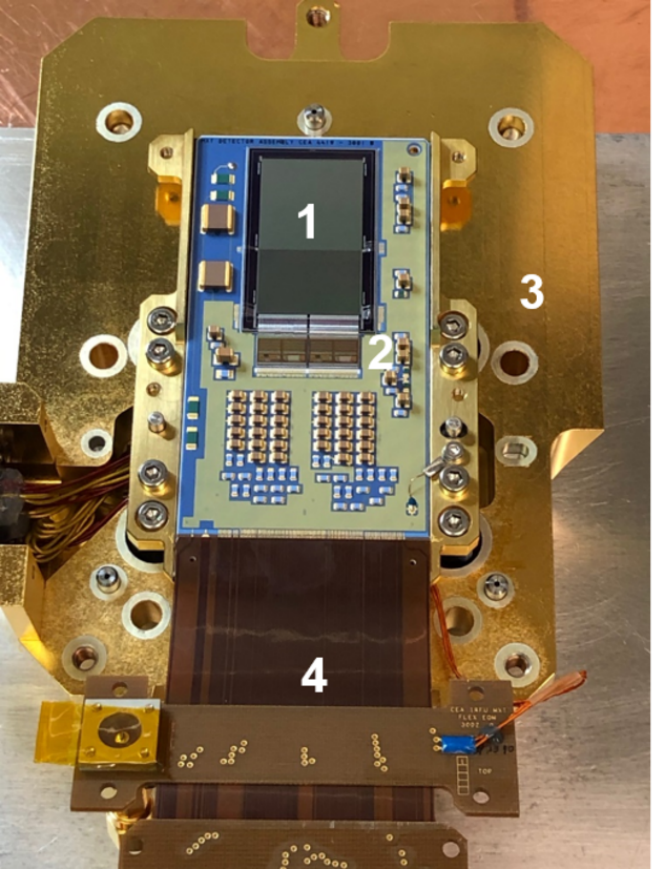
1
2
3
4

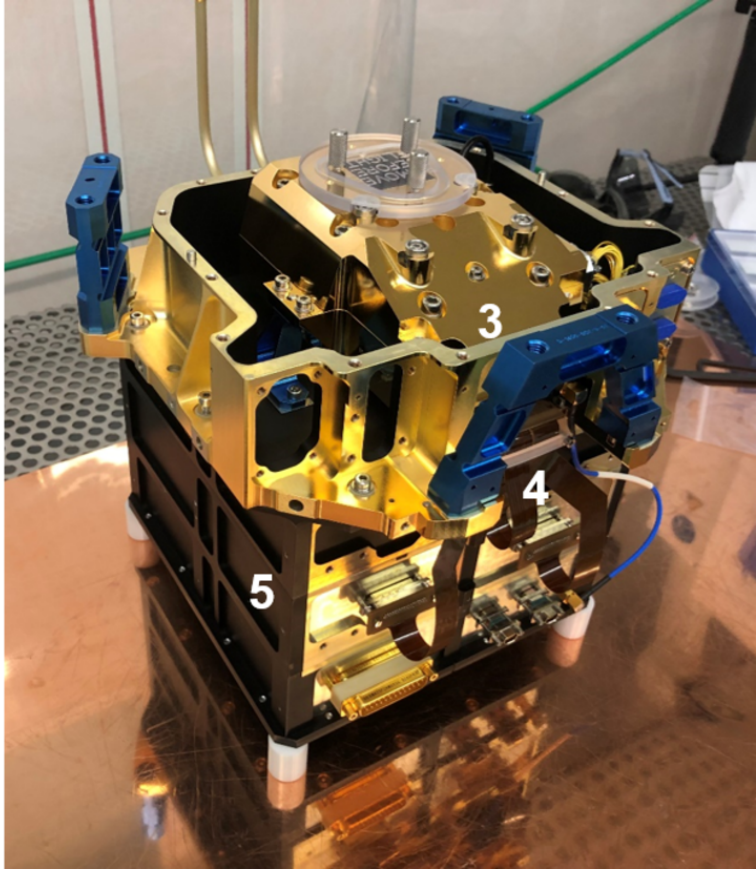
3
4
5

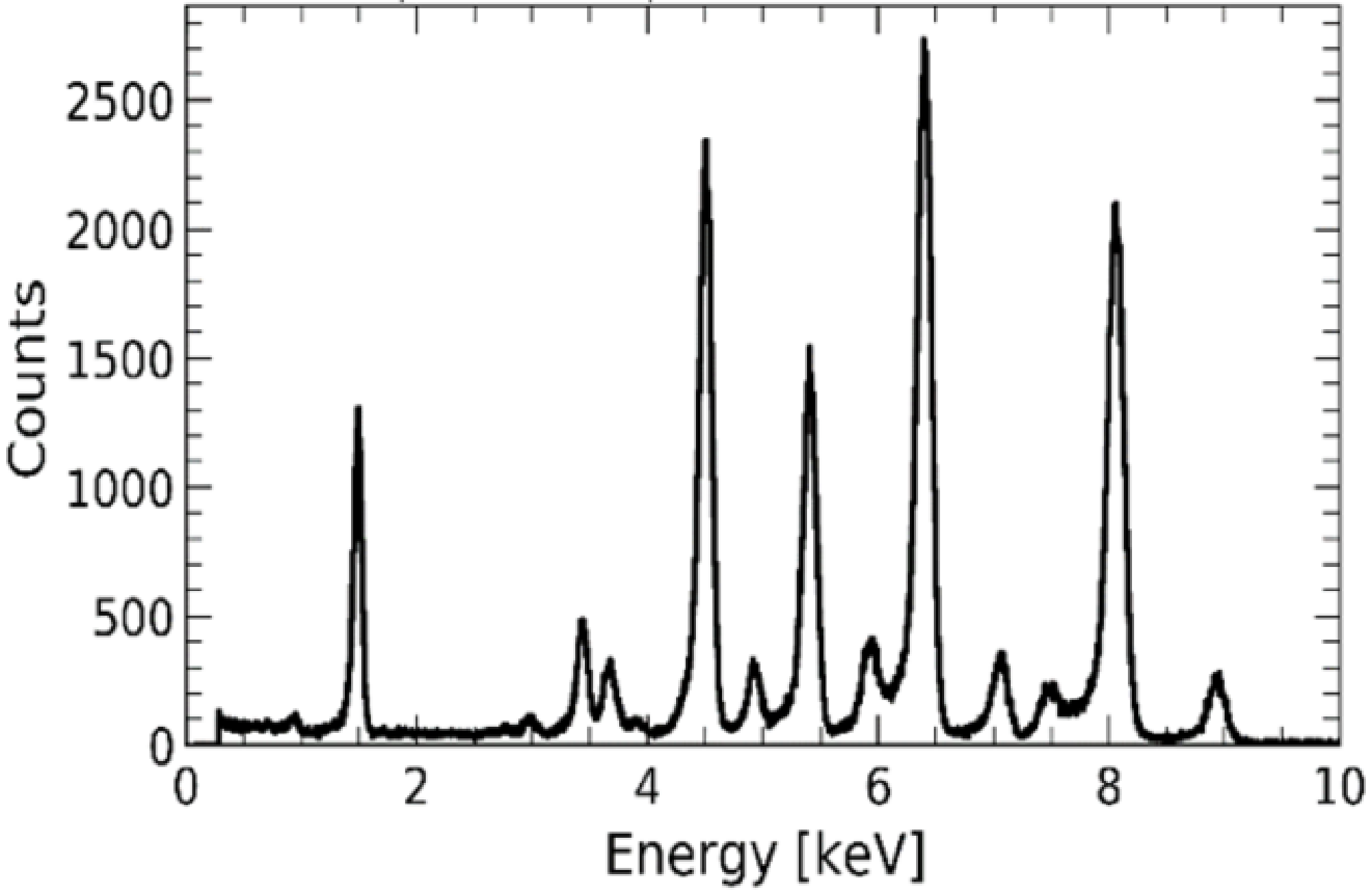
Counts
2500
2000
1500
1000
500
0
0
2
4
6
8
10
Energy [keV]

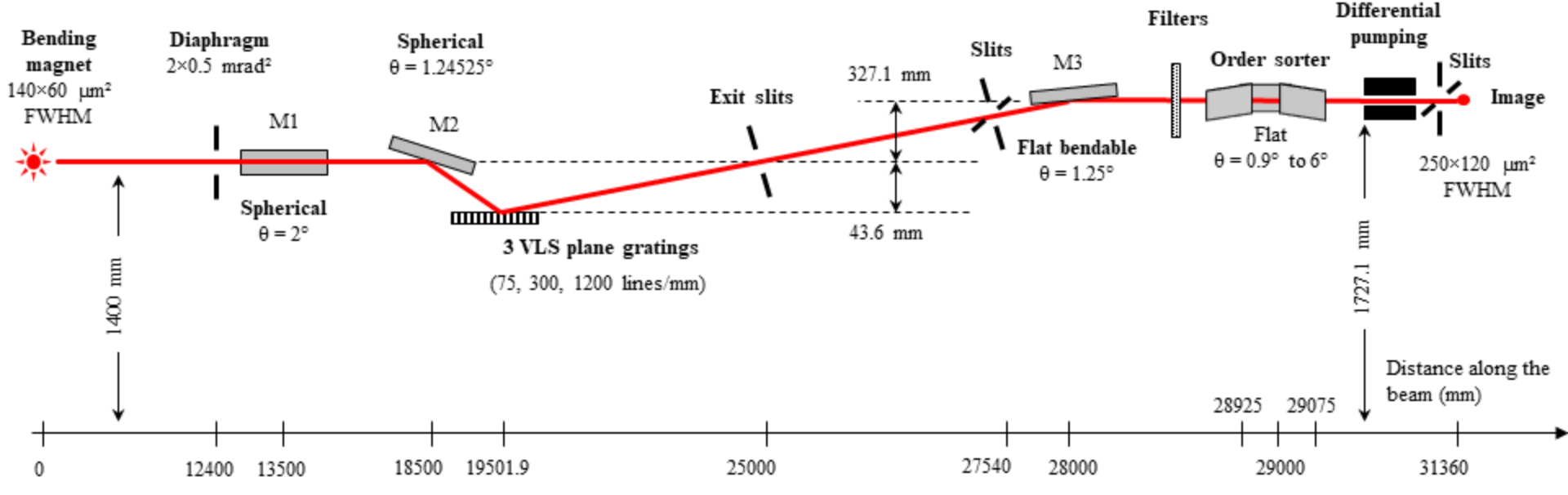
Bending magnet
140×60 µm² FWHM
Diaphragm
2×0.5 mrad²
M1
Spherical
θ = 2°
Spherical
θ = 1.24525°
M2
3 VLS plane gratings
(75, 300, 1200 lines/mm)
Exit slits
327.1 mm
43.6 mm
Slits
M3
Flat bendable
θ = 1.25°
Filters
Order sorter
Flat
θ = 0.9° to 6°
Differential pumping
Slits
Image
250×120 µm² FWHM
1400 mm
1727.1 mm
Distance along the beam (mm)
0
12400
13500
18500
19501.9
25000
27540
28000
28925
29075
29000
31360

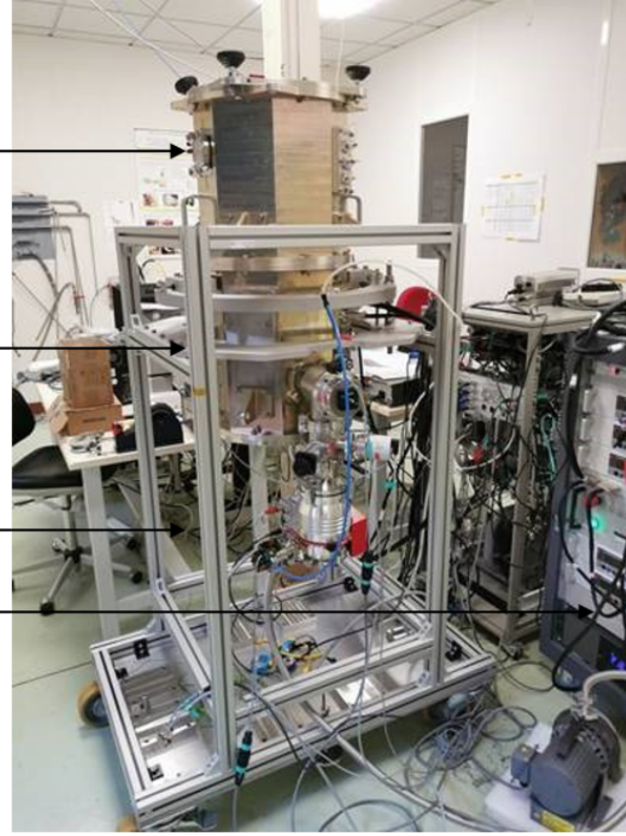
Entrance window
(Beam axis)
Trolley with
alignment
systems
Turbopump
Control racks

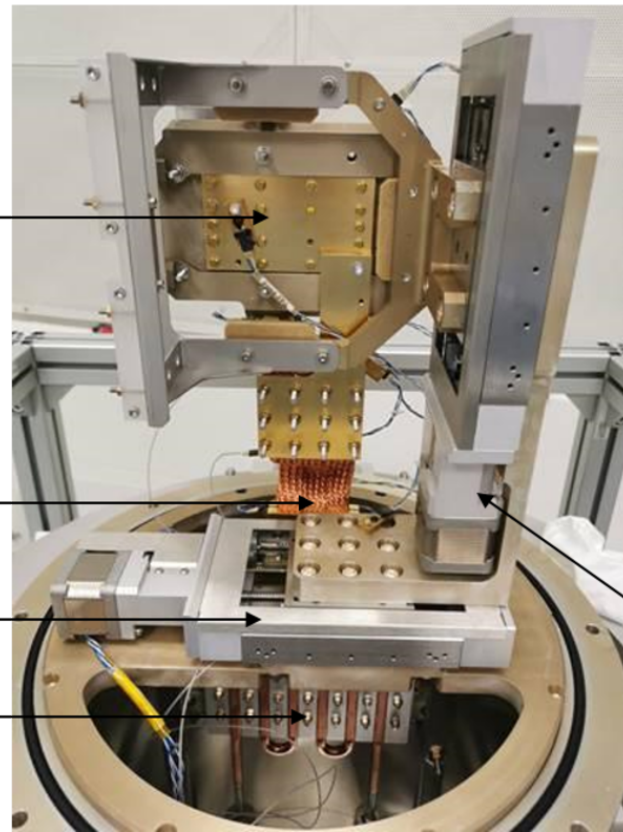
Focal plane
Thermal link
Displacement tables
Cooling plate

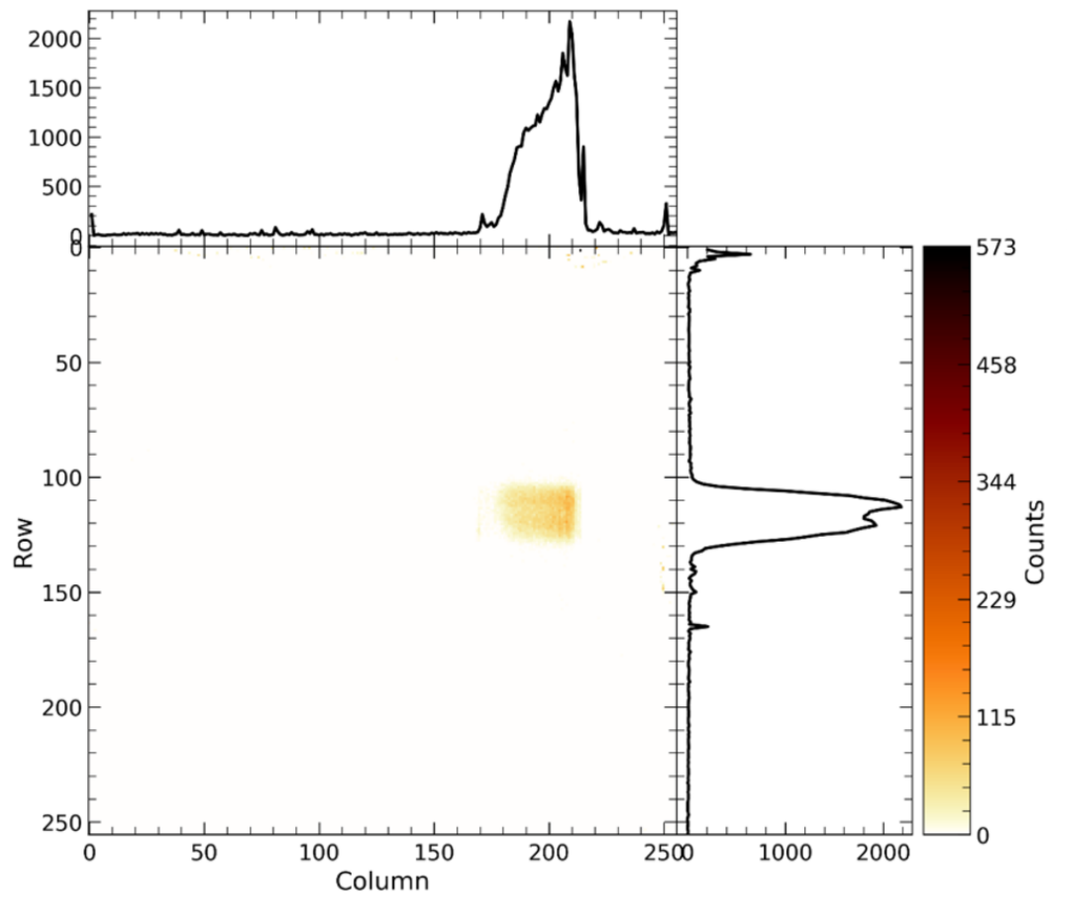
Row
Column
Counts
573
458
344
229
115
0

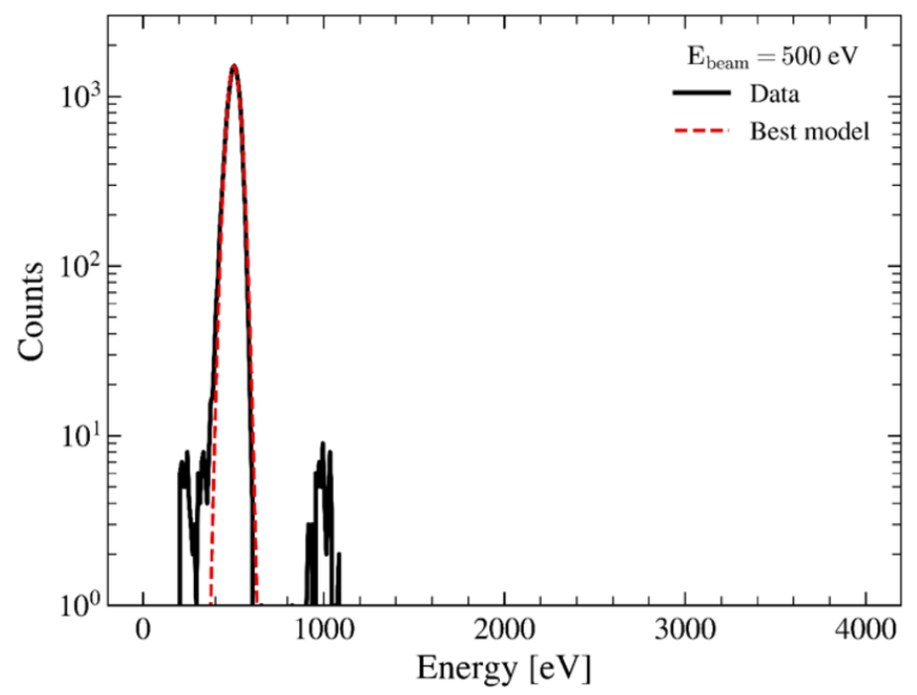
$E_{beam} = 500$ eV
Data
Best model
Counts
Energy [eV]

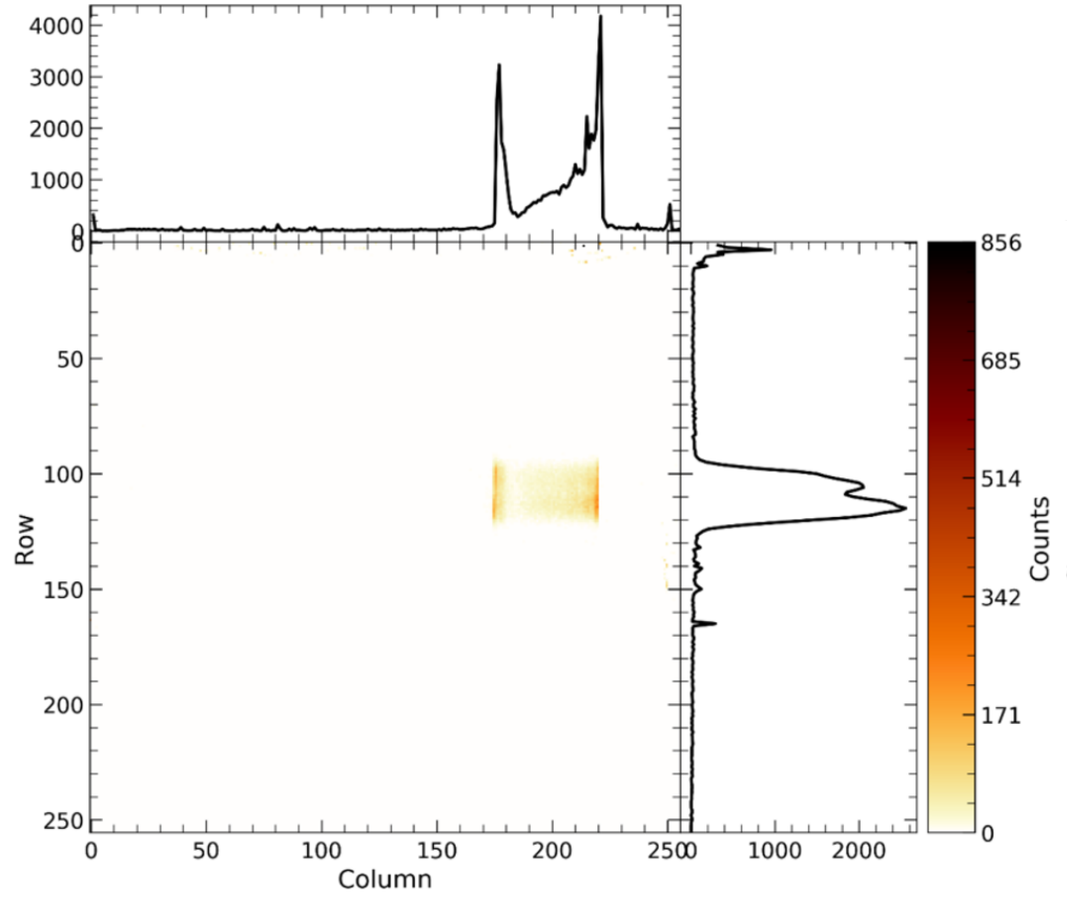
Row
Column
Counts
856
685
514
342
171
0

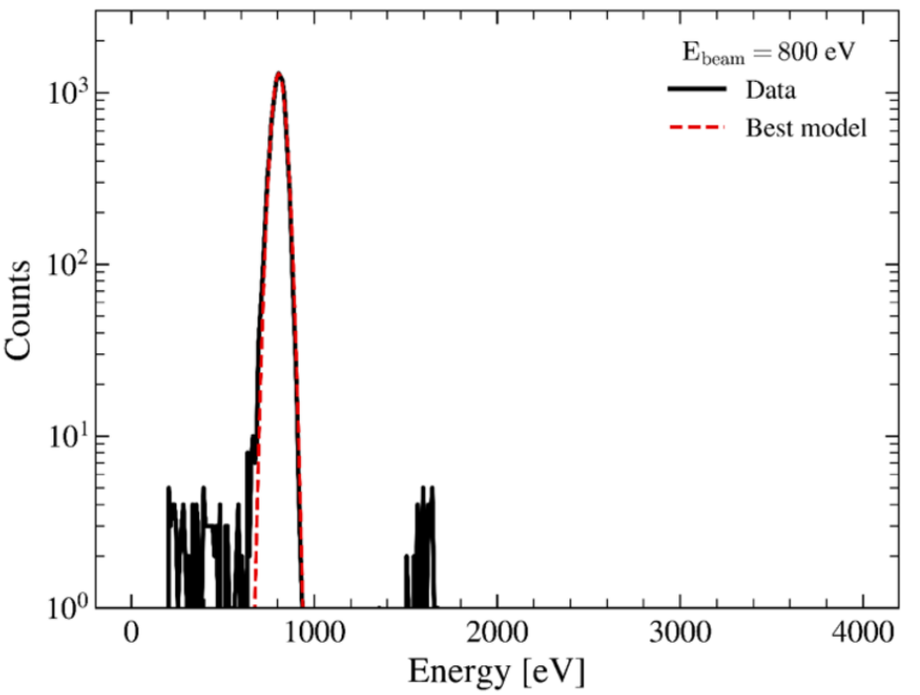
$E_{beam} = 800$ eV
Data
Best model
Counts
Energy [eV]

Model MXT
Singles
Doubles
Triples
Quadruples
Fraction
0.8
0.6
0.4
0.2
0.0
0.1
1
Energy [keV]

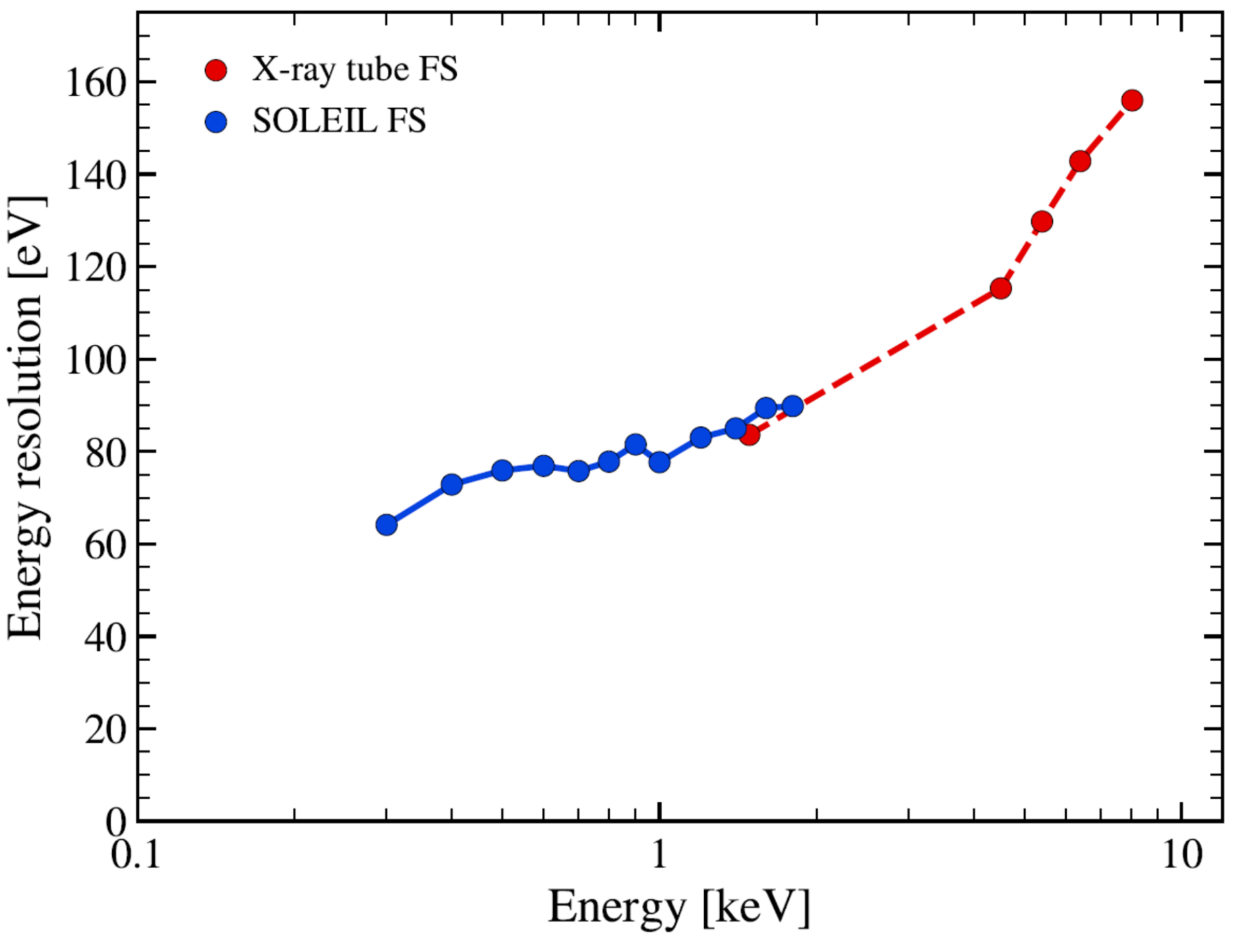
X-ray tube FS
SOLEIL FS
Energy resolution [eV]
Energy [keV]
0
20
40
60
80
100
120
140
160
0.1
1
10

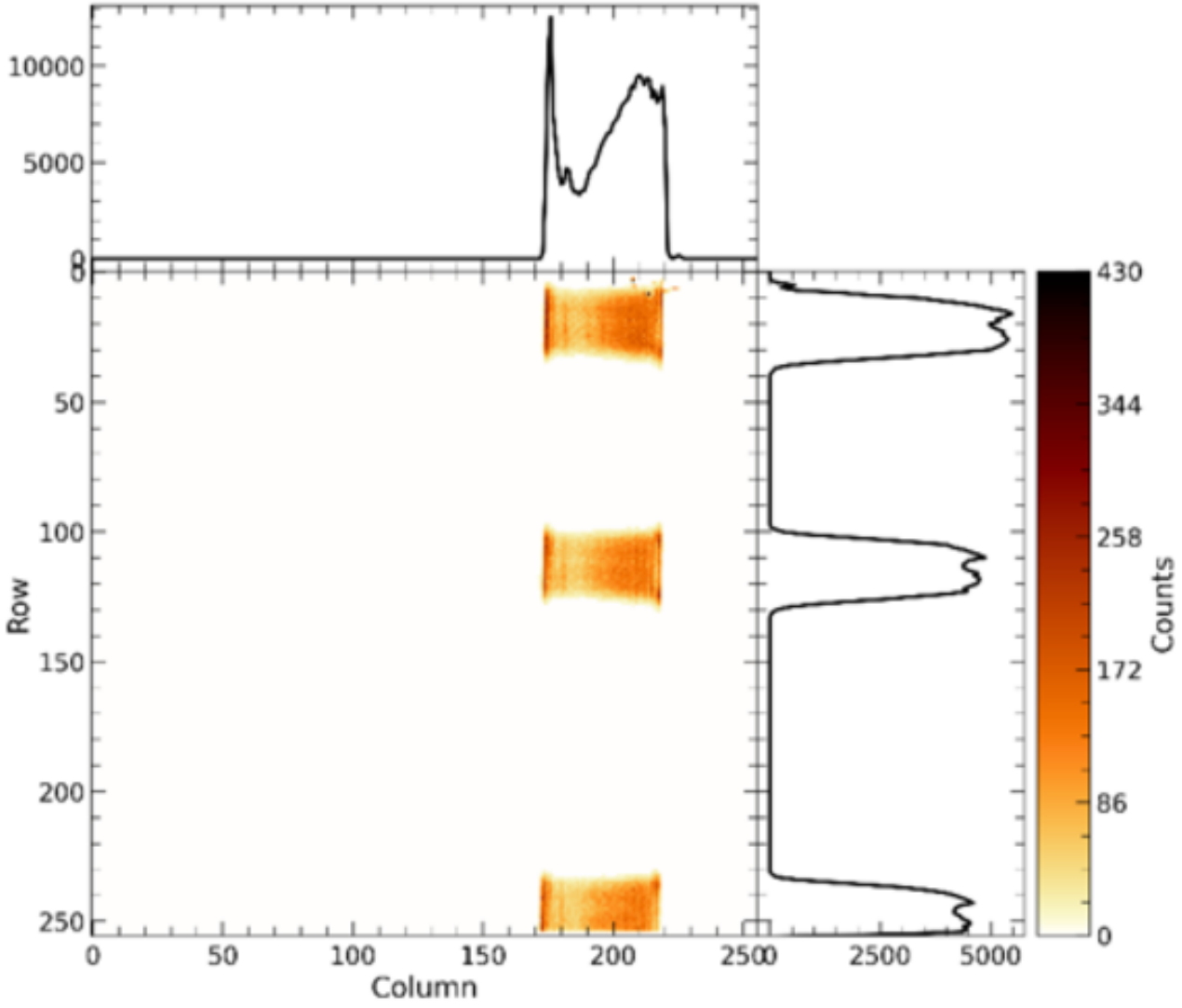
10000
5000
0
Row
50
100
150
200
250
0
50
100
150
200
2500
2500
5000
Column
430
344
258
172
86
0
Counts

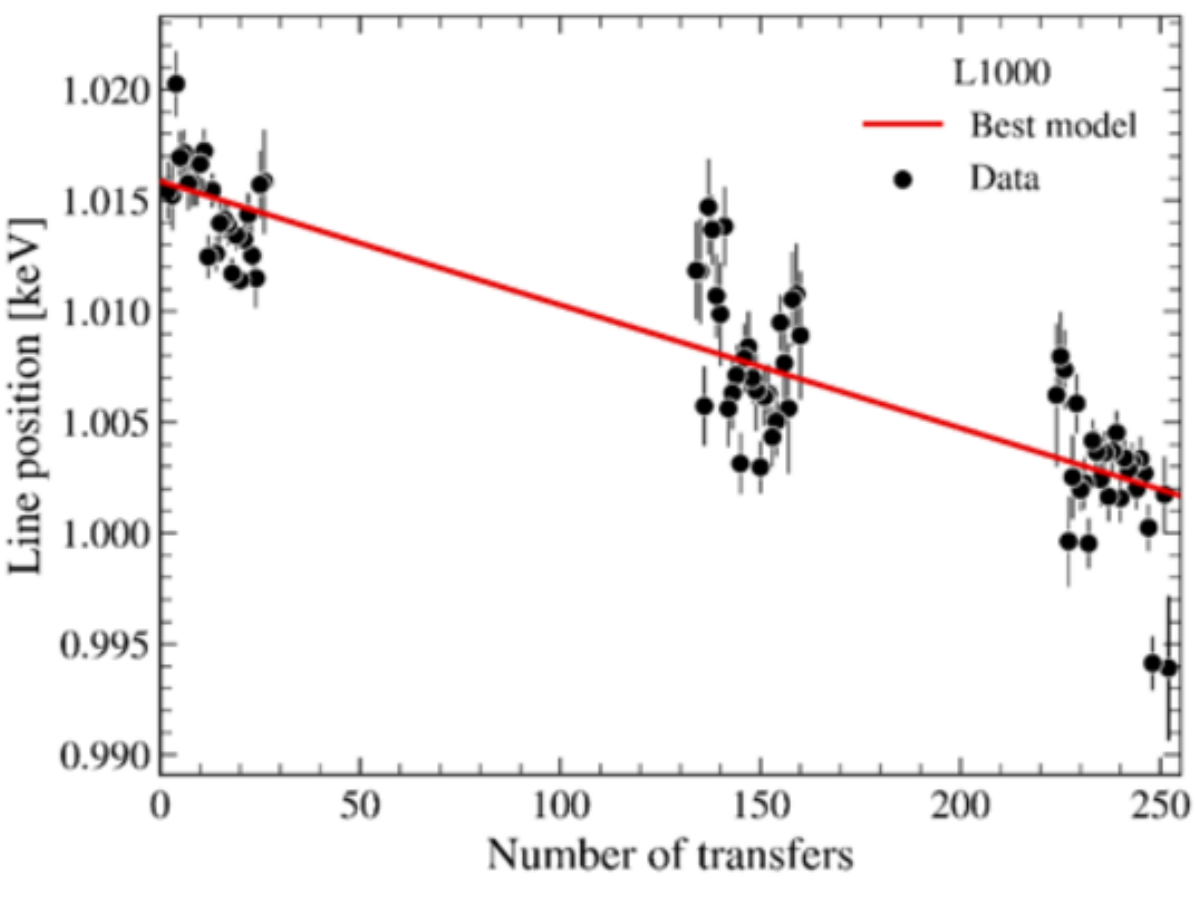
L1000
Best model
Data
Line position [keV]
1.020
1.015
1.010
1.005
1.000
0.995
0.990
0
50
100
150
200
250
Number of transfers

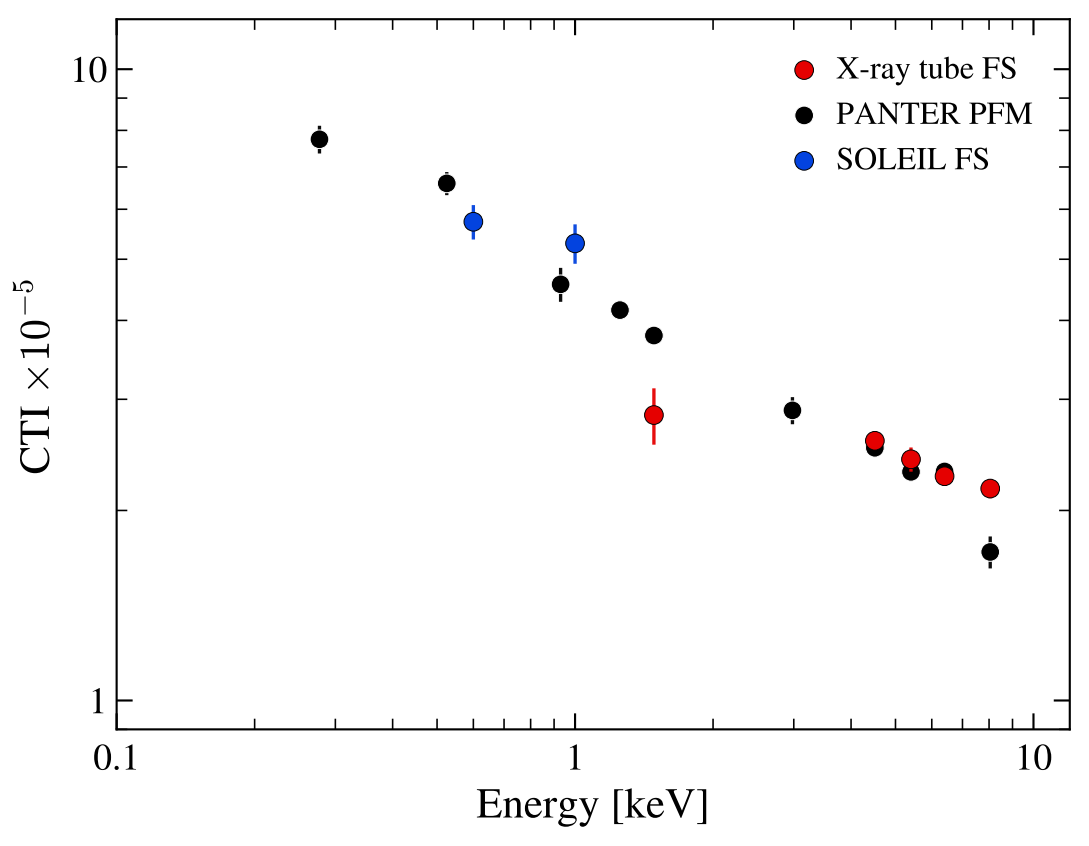
X-ray tube FS
PANTER PFM
SOLEIL FS
CTI $\times 10^{-5}$
10
1
0.1
1
10
Energy [keV]

(a)

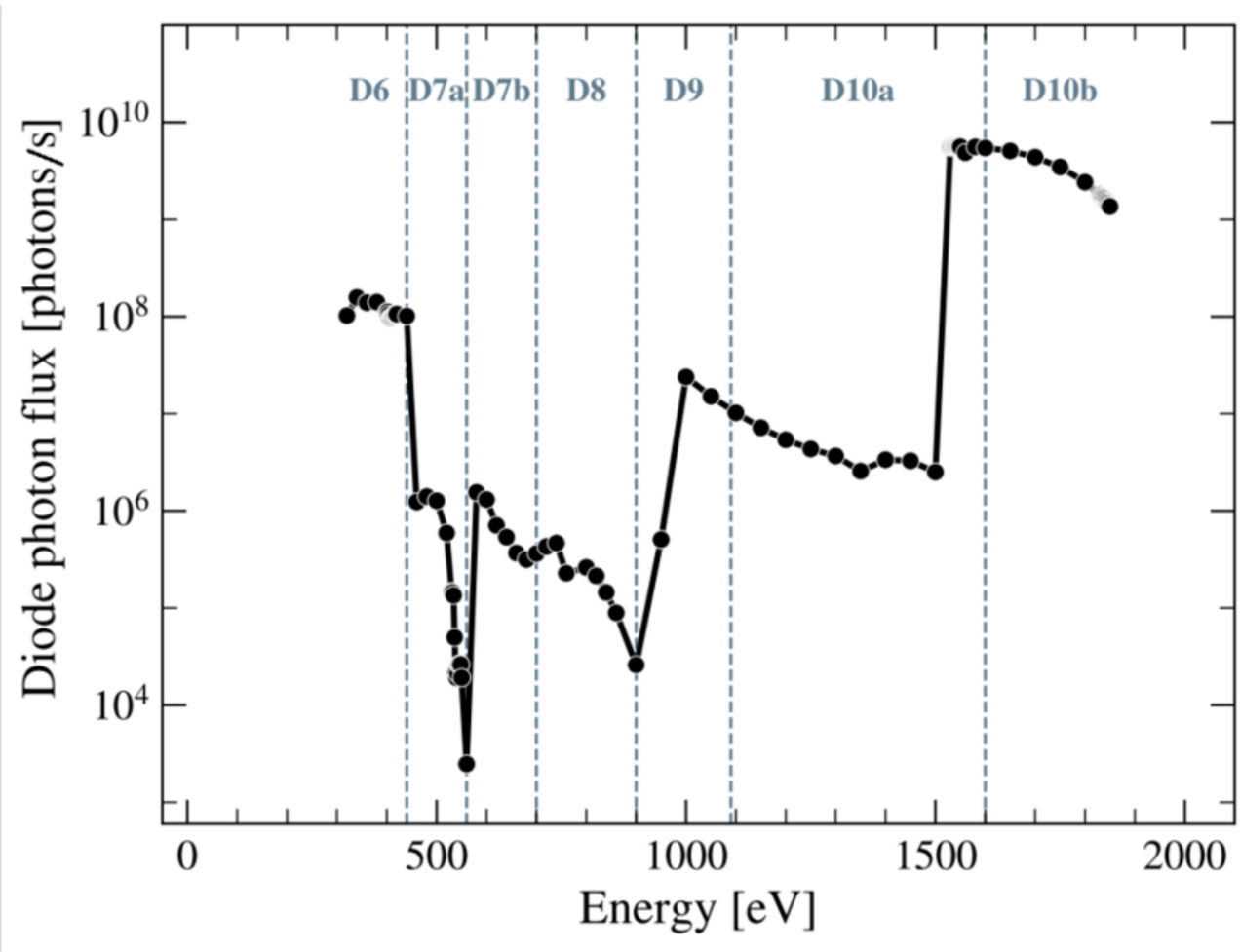
D6
D7a
D7b
D8
D9
D10a
D10b
Diode photon flux [photons/s]
10^{10}
10^{8}
10^{6}
10^{4}
0
500
1000
1500
2000
Energy [eV]

(b)

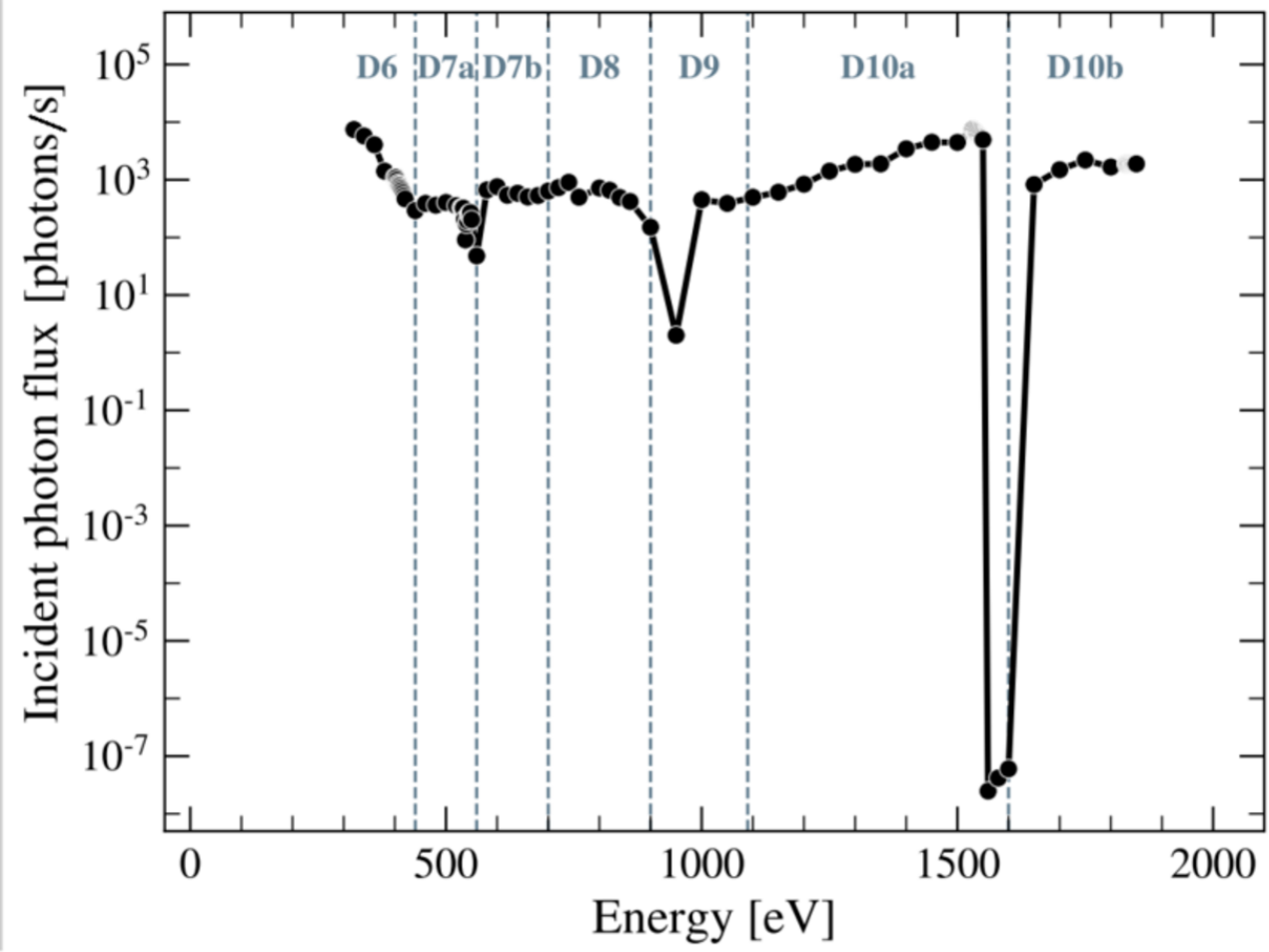
D6
D7a
D7b
D8
D9
D10a
D10b
Incident photon flux [photons/s]
10^{5}
10^{3}
10^{1}
10^{-1}
10^{-3}
10^{-5}
10^{-7}
0
500
1000
1500
2000
Energy [eV]

(c)

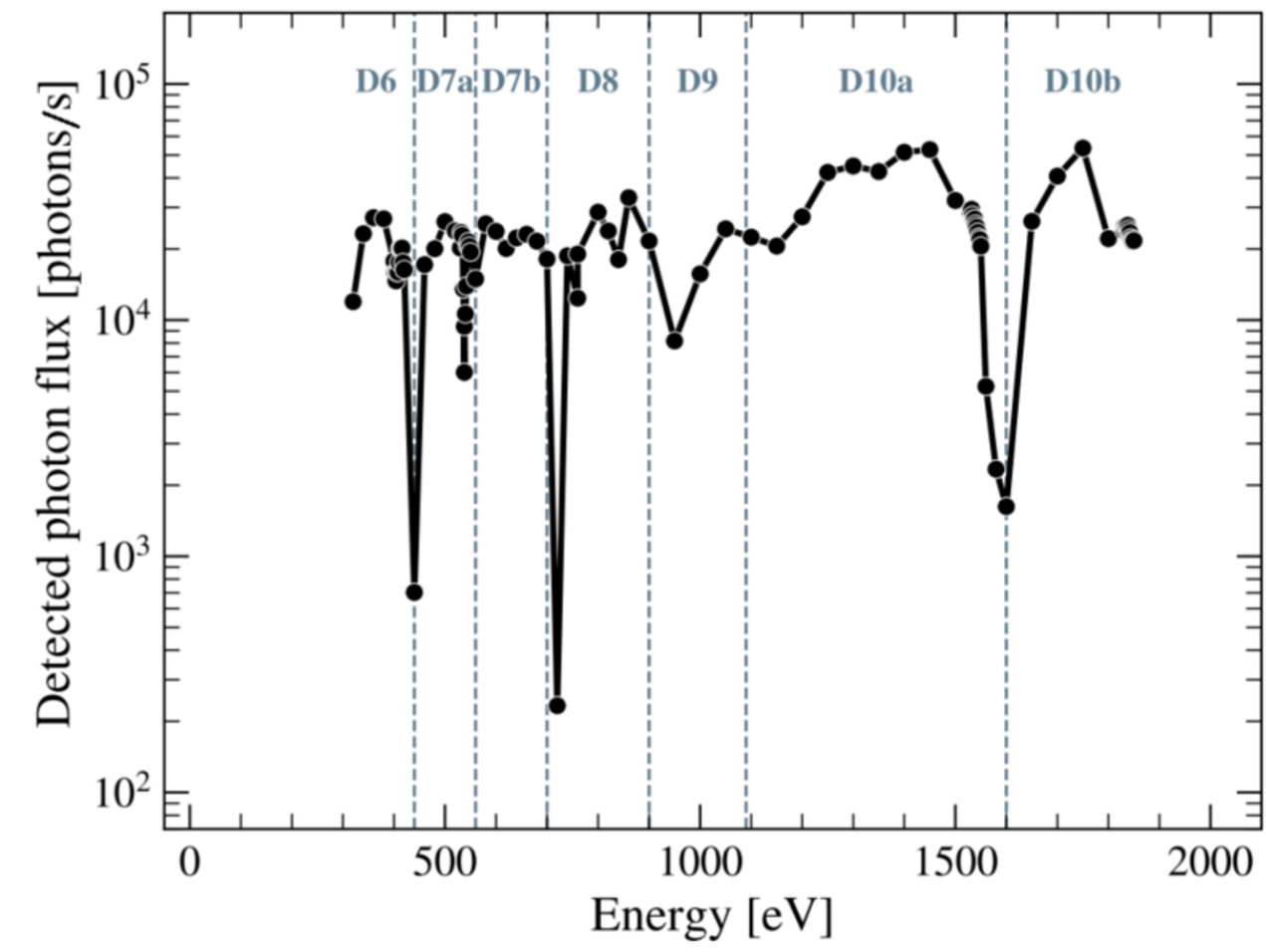
D6
D7a
D7b
D8
D9
D10a
D10b
Detected photon flux [photons/s]
10^{5}
10^{4}
10^{3}
10^{2}
0
500
1000
1500
2000
Energy [eV]

Figure 1: SVOM astrophysics mission, composed of a space segment with 4 instruments and a ground segment with 3 robotic telescopes (left) to cover the spectral domain from the infrared to the gamma-ray range and time scales from seconds to days (right).

Figure 2: Focal plane assembly (FPA) of the MXT camera. A ceramic board equipped with a pnCCD (1) and 2 Camex ASIC (2) is mounted in a proton shielding (3) and the flex lead (4) is connected to the warm front-end electronics (5).

Figure 3: Sum spectrum of single events produced with the MXT FPA cryostat equipped with a full custom X-ray source. This source is composed of an X-ray tube hitting a composite target. X-ray fluorescence lines are produced at 1.49 keV (Al K_α), 3.44 keV, 3.77 keV (Sn K_α and K_β), 4.51 keV, 4.93 keV (Ti K_α and K_β), 5.41 keV, 5.95 keV (Cr K_α and K_β), 6.40 keV, 7.06 keV, (Fe K_α and K_β), 7.47 keV (Ni K_α), 8.04 keV and 8.91 keV (Cu K_α and K_β). The best energy resolution measured in the initial configuration of the cryostat is 79 eV FWHM at 1.49 keV at -65°C; the energy resolution in the refurbished cryostat prior to the SOLEIL test campaign was measured to be 84 eV FWHM at 1.5 keV at the same temperature.

Figure 4 : Optical scheme of the soft X-ray branch of the Metrology beamline of SOLEIL synchrotron.

Figure 5 : MXT Cryostat (Top) outer part (Bottom) inner part.

Figure 6 : Count maps and spectra with single events and global energy calibration for a beam at 500 eV (top) and at 800 eV (bottom). For each energy, the fraction of counts at twice the nominal energy is below 1 %. The different shape of the image at 800 eV compared to that at 500 eV is due to the smaller slit opening (2 µm instead of 8 µm).

Figure 7 : Statistics of the event multiplicity measured at SOLEIL and modeling of the charge sharing in the MXT detector operated at -60°C with an average low-level threshold of 46 eV. The incoherent result at 300 eV is explained by the experimental setup causing spurious events at low energy that are not photons and that corrupt the photon statistics.

Figure 8 : Comparison of the energy resolution of single events measured at SOLEIL and in the lab with the MXT flight spare detection chain.

Figure 9 : (Top) Data set to extract the CTE at 1000 eV. The detector was illuminated on three positions aligned along the columns. (Bottom) The line position is estimated row by row from a global energy calibration, and the slope of the line position with the number of transfers gives the charge transfer inefficiency using Equation (5).

Figure 10 : Comparison of the charge transfer inefficiency measured at SOLEIL (blue) and in the lab with the Flight spare detection chain (red). Data with the flight model from the same production batch were also obtained during the instrument calibration at PANTER [6] (black).

Figure 11 : (a) Photon flux measured by the diode according to equation 1. (b) Incident flux on the detector reconstructed according to equation 2. (c) Detected flux recorded by the detector. Between two dotted lines (one energy band), the filter configuration of the beamline is unchanged, only the slit opening is modified while scanning the energy points.

Table 1: Configurations used to ensure a photon flux of ~ 200 photons/s in the beam for the MXT measurements. The incident flux on MXT was estimated from measurements given by a reference photodiode and obtained in a beamline configuration as close as possible to the one used for the MXT measurements. The gratings and the beamline filter represented in the Figure 4 are identical for the two detectors for each energy band and are not specified here. The angle of the low-pass filter (LPF) is increased for MXT measurements in some cases to reduce flux. The slits opening is also adjusted for each energy within the energy band to avoid pile-up.

Band reference	Energy (eV)	MXT detector			Reference silicon diode		
		LPF angle	Slits (µm)	External Filter	LPF angle	Slits (µm)	External Filter
D6	300-440	Cr 5.5°	15 – 100	0.5 µm Co	Cr 2.5°	100	∅
D7a	460-560	Si 3.2°	8 – 100	0.5 µm Co	Si 3.2°	100	∅
D7b	560-700	Si 2.2°	2 – 3	0.5 µm Co	Si 2.2°	100	∅

D8	760-900	Si 2.1°	2 – 2.5	0.9 µm Cu	Si 2.1°	100	∅
D9	910-1090	Si 1.2°	4 – 40	0.9 µm Cu	Si 1.8°	100	∅
D10a	1100-1550	Si 1.1°	2 – 2.5	25 µm Al	Si 1.1°	100	∅
D10b	1600-1800	∅	2 – 7	5 µm Co	∅	100	∅